MATERIALS CHEMISTRY FRONTIERS

RESEARCH ARTICLE

View Article Online
View Journal | View Issue

Cite this: *Mater. Chem. Front.*, 2023, **7**, 1684

Facile synthesis of 2D Al-TCPP MOF nanosheets for efficient sonodynamic cancer therapy†

Zhan Zhou, ‡[a] Tao Wang,‡[b] Tingting Hu,‡[b] Chunhua Cheng,[a] Shilong Yu,[c] Hai Li,[c] Shuyan Liu,[d] Lufang Ma, *[a] Meiting Zhao, *[e] Ruizheng Liang*[b] and Chaoliang Tan *[fg]

Two-dimensional (2D) metal–organic framework (MOF) nanosheets have been widely explored in recent years as diagnostic and therapeutic reagents for cancer therapies, including photodynamic therapy, chemodynamic therapy, radiation therapy, and catalytic therapy, because of their appealing physicochemical properties. Herein, we report the first preparation of 2D Al-TCPP (TCPP: tetrakis(4-carboxyphenyl)porphyrin) MOF nanosheets, for use as an effective sonosensitizer for sonodynamic cancer therapy, *via* a simple solvothermal synthesis method without the need for any surfactants. The 2D Al-TCPP nanosheets have a size of 160–200 nm and a thickness of 18.4–26.5 nm and were synthesized by changing the ratio of water to *N*,*N*-dimethylformamide. Interestingly, other organic solvents, such as dimethylacetamide, dimethyl sulfoxide, and *N*-methyl-2-pyrrolidone, can be also used as the co-solvent for the facile synthesis of the 2D Al-TCPP nanosheets. Promisingly, the Al-TCPP nanosheets generate a much higher yield of reactive oxygen species (*i.e.*, singlet oxygen ($^1O_2$) and hydroxyl radical (•OH)) under ultrasound treatment than free TCPP molecules, suggesting that embedding the TCPP molecules in the 2D Al-TCPP nanosheets could significantly enhance the sonodynamic cancer therapeutic activity. Both the *in vitro* and *in vivo* results prove that, after modification with polyethylene glycol, the Al-TCPP nanosheets can be used as a sonosensitizer for efficient sonodynamic therapy to kill cancer cells and eliminate malignant tumors.

Received 21st December 2022,
Accepted 27th February 2023

DOI: 10.1039/d2qm01333a

rsc.li/frontiers-materials

Introduction

Sonodynamic therapy (SDT) is a new non-invasive treatment strategy that has been increasingly applied in biomedical fields, including in cancer therapy and antibacterial therapy due to its ability to generate toxic reactive oxygen species (ROS) under ultrasound (US) radiation.[1–8] Like photodynamic therapy (PDT), SDT also needs the participation of a sonosensitizer, which can convert the low-frequency ultrasonic waves into chemical energy that produces the ROS for effective destruction of cancer cells in deep tumors.[9–12] Therefore, the sonosensitizer plays a decisive role in the ultrasonic efficiency of the SDT process. Sonosensitizers that have been developed to date can be mainly divided into two categories: inorganic semiconductor nanomaterials and highly conjugated organic molecules. Titanium-based nanomaterials (*e.g.*, TiO_2, TiO_{2-x}, TiN, and TiH) are a class of inorganic sonosensitizers that have been widely used for SDT due to their excellent stability and tunable multifunctionality,[13–23] while their insufficient US absorption coefficient limits their treatment effectiveness. Compared to the inorganic sonosensitizers, some organic molecules (*e.g.*, near-infrared dyes, porphyrins and their derivatives) exhibit good biocompatibility and sonodynamic properties because their large conjugated structures improve the quantum yield of the ROS during US treatment.[24–30] However, organic sonosensitizers normally suffer from unsatisfactory hydrophilicity and photobleaching, thus limiting their practical development. Introducing organic sonosensitizers into a porous framework to construct an ordered framework material

[a] *College of Chemistry and Chemical Engineering, Henan Key Laboratory of Function-Oriented Porous Materials, Luoyang Normal University, Luoyang, 471934, China. E-mail: mazhuxp@126.com*
[b] *State Key Laboratory of Chemical Resource Engineering, Beijing Advanced Innovation Center for Soft Matter Science and Engineering, Beijing University of Chemical Technology, Beijing, 100029, China. E-mail: liangrz@mail.buct.edu.cn*
[c] *Institute of Advanced Materials (IAM) and Key Laboratory of Flexible Electronics (KLoFE), Nanjing Tech University (NanjingTech), 30 South Puzhu Road, Nanjing, 211816, China*
[d] *Department of Endocrinology, The First Affiliated Hospital of Henan Polytechnic University (Jiaozuo Second People's Hospital), Jiaozuo, China*
[e] *Department of Chemistry, Institute of Molecular Aggregation Science, Tianjin Key Laboratory of Molecular Optoelectronic Sciences, Tianjin University, Tianjin, 300072, China. E-mail: mtzhao@tju.edu.cn*
[f] *Department of Chemistry and Center of Super-Diamond and Advanced Films (COSDAF), City University of Hong Kong, Kowloon, Hong Kong SAR 999077, China. E-mail: chaoltan@cityu.edu.hk*
[g] *Shenzhen Research Institute, City University of Hong Kong, Shenzhen, 518057, China*

† Electronic supplementary information (ESI) available. See DOI: https://doi.org/10.1039/d2qm01333a

‡ These authors contributed equally to this work.

can effectively improve the solubility and photostability of organic sonosensitizers, which is expected to enhance their SDT performance.

Metal–organic frameworks (MOFs) are a class of porous ordered framework material that have been widely applied in various fields due to their remarkable physical and chemical properties, including high porosity, the possession of multiple active sites, high specific surface area, tunable morphology, and excellent biodegradability.[31–53] Recently, some porphyrin-based sonosensitizers (*e.g.*, HMME: hematoporphyrin monomethyl ether, and TCPP: tetrakis(4-carboxyphenyl)porphyrin) have been used as organic ligands to assemble MOFs with various metal ions (*e.g.*, Fe^{3+}, Zr^{4+}, Cu^{2+}, Ti^{4+}, and Al^{3+}) for SDT against bacterial and cancer targets.[54–62] Fe-HMME coordination particles were the first example of a MOF-based sonosensitizer, and are assembled *via* coordination bonds between a clinical drug (*i.e.*, HMME) and Fe^{3+}. The pores of the Fe-HMME coordination particles can effectively adsorb anticancer drug (DOX: doxorubicin) with high loading efficiency for sonodynamic-chemo combined therapy.[54] Since this first report, although different kinds of MOF-based sonosensitizers have been explored for SDT, they have mainly focused on nanoparticles, which exhibit low SDT performance and thus have to be combined with other treatment strategies, including PDT, chemodynamic therapy (CDT), chemotherapy, gas therapy, and gene therapy, for completely effective elimination of the tumors. However, the sonodynamic properties of two-dimensional (2D) MOF nanosheet-based sonosensitizers and their applications in sonodynamic cancer therapy have not yet been reported.

Herein, we report the facile synthesis of 2D Al-TCPP MOF nanosheets through a simple solvothermal method, without the addition of any surfactants, for enhanced SDT (Fig. 1). The 2D nanosheet morphology of Al-TCPP can be easily controlled by changing the ratio of water and organic solvent, while a wide range of common organic solvents can be used, including *N*,*N*-dimethylformamide (DMF), dimethylacetamide (DMAC), dimethyl sulfoxide (DMSO), and *N*-methyl-2-pyrrolidone (NMP). Compared with free TCPP molecules, the 2D Al-TCPP MOF nanosheets result in much higher singlet oxygen ($^1O_2$) and hydroxyl radical ($^{\bullet}OH$) quantum yields under the same US treatment conditions, and thus they can be used as efficient sonosensitizers for enhanced SDT. After modification with polyethylene glycol (PEG), the PEG@Al-TCPP MOF nanosheets exhibit better SDT activity than that of free TCPP, both *in vitro* and *in vivo*. Therefore, the PEG@Al-TCPP MOF nanosheets can act as an efficient sonosensitizer for enhanced sonodynamic cancer therapy.

Results and discussion

The 2D Al-TCPP MOFs were prepared *via* a typical solvothermal synthesis method using a mixed solvent of DMF and deionized (DI) water (see the Experimental section). The morphology and size of the MOFs can be effectively controlled by only adjusting the content of organic solvent. As shown in the scanning

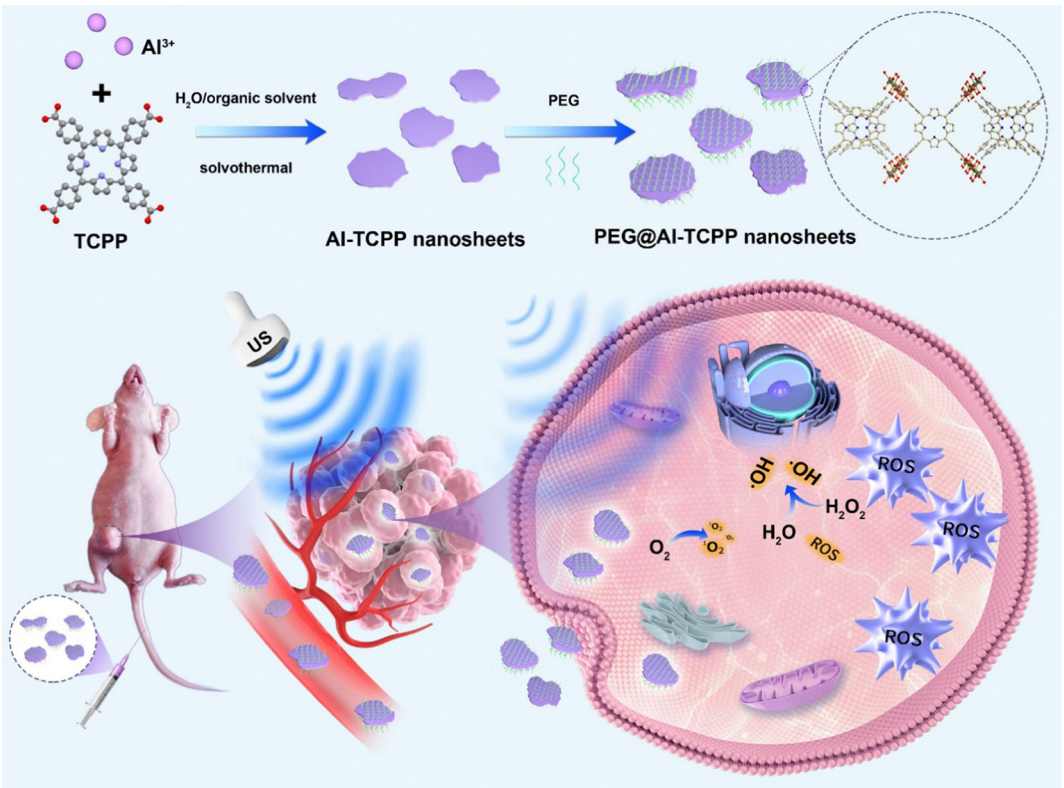

Fig. 1 Schematic illustration of the 2D PEG@Al-TCPP nanosheets, efficient sonosensitizers for sonodynamic cancer therapy.

electron microscopy (SEM) images, the Al-TCPP MOFs exhibit a regular nanobelt morphology with a length of up to 500–700 nm and a width of 80–100 nm when 1 mL of DMF and 3 mL of DI water are used as the reaction solvent (Fig. S1a, ESI†). The proportion of nanobelts is reduced and accompanied by the formation of some nanosheets after reducing the amount of DMF from 1 to 0.8 mL (Fig. S1b, ESI†). More interestingly, uniform and regular nanosheets with a size of 160–200 nm were obviously visible in the SEM images (Fig. 2a and b) of the Al-TCPP MOFs prepared *via* the same procedure except with a volume of 0.5 mL of DMF, thus indicating that the synthesis of the 2D Al-TCPP nanosheets could be controlled by adjusting the volume of DMF employed in the solvothermal method. To explore the universality of this synthetic method, some other organic solvents (*e.g.*, DMAC, DMSO, NMP) were used to prepare the Al-TCPP MOFs. As shown in Fig. S2 (ESI†), all the samples synthesized when using DMAC, DMSO, and NMP exhibited regular nanosheets, except their average size was smaller than that of the Al-TCPP nanosheets made from the DMF protocol, demonstrating that the type of organic solvent used could effectively control the morphology of the 2D Al-TCPP nanosheets. Moreover, the morphology of the 2D Al-TCPP nanosheets was further studied using transmission electron microscopy (TEM). The TEM image of the obtained 2D Al-TCPP nanosheets (Fig. 2c) displays the same regular nanosheets that are seen in the SEM image (Fig. 2b). The high-resolution TEM (HRTEM) image of the 2D Al-TCPP nanosheets exhibits a continuous crystal lattice fringe (Fig. 2d), suggesting that the nanosheets have excellent crystallinity. The lattice distance was measured to be 1.59 nm, which was attributed to the (200) planes of the Al-TCPP crystal.[63] The crystallinity of the 2D Al-TCPP nanosheets was further demonstrated by their selected area electron diffraction (SAED) pattern, which shows a diffraction ring with bright spots (Fig. 2e). The thickness of the 2D Al-TCPP nanosheets was measured to be 18.4–26.5 nm from its atomic force microscopy (AFM) image (Fig. 2f and Fig. S3, ESI†).

The crystal structure of the 2D Al-TCPP nanosheets was further characterized using X-ray powder diffraction (XRD). All the XRD peaks of the 2D Al-TCPP nanosheets match well with the simulated peaks from its crystal structure (Fig. S4, ESI†), suggesting that 2D Al-TCPP nanosheets possessed good crystallinity and the original structure of the Al-TCPP MOFs crystal remained intact. In addition, the 2D Al-TCPP nanosheets were also characterized using X-ray photoelectron spectroscopy (XPS). The high-resolution XPS C 1s spectrum of the Al-TCPP nanosheets exhibited two main peaks located at 284.8 and 288.8 eV (Fig. S5a, ESI†), which were attributed to C═C and C–O, respectively. Signals at 397.2 and 399.4 eV were observed in the N 1s XPS spectrum (Fig. S5b, ESI†), assignable to C═N and C–N, respectively. As shown in the O 1s and Al 2p XPS spectra of the Al-TCPP nanosheets (Fig. S5c and d, ESI†), the peaks at 532.2 and 74.6 eV correspond to the Al–O bond, suggesting the presence of elemental aluminum. Therefore, the above results verified the successful assembly of the 2D Al-TCPP nanosheets. In addition, the porosity of the 2D Al-TCPP nanosheets was determined by means of N_2 adsorption isotherm analysis at 77 K. As shown in Fig. S6 (ESI†), the Brunauer–Emmett–Teller (BET) surface area and pore size of the 2D Al-TCPP nanosheets were calculated to be 1303 $m^2\ g^{-1}$ and 0.75 nm, respectively. This excellent specific surface area could provide the Al-TCPP nanosheets with a large active area to improve its generation of ROS during US treatment.

We tested the catalytic activity of Al-TCPP for $^1O_2$ generation under US irradiation (50 kHz, 1.6 W cm^{-2}) using a singlet

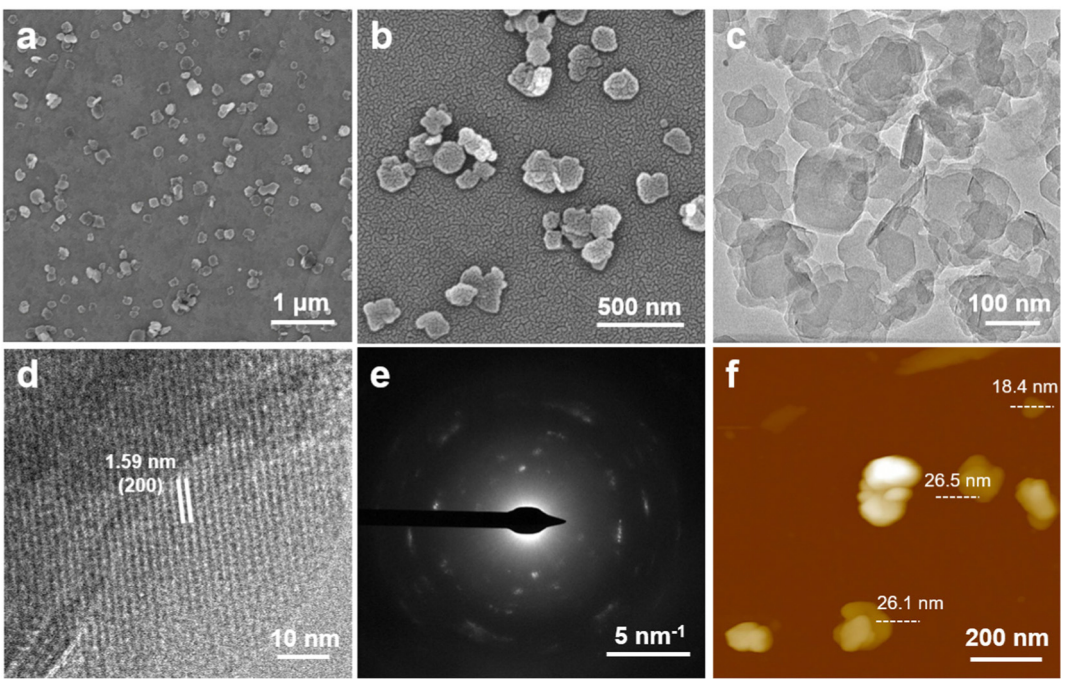

Fig. 2 (a and b) SEM and (c) TEM images of the 2D Al-TCPP nanosheets. (d) HRTEM image and (e) SAED pattern of typical 2D Al-TCPP nanosheets. (f) AFM height image of the 2D Al-TCPP nanosheets.

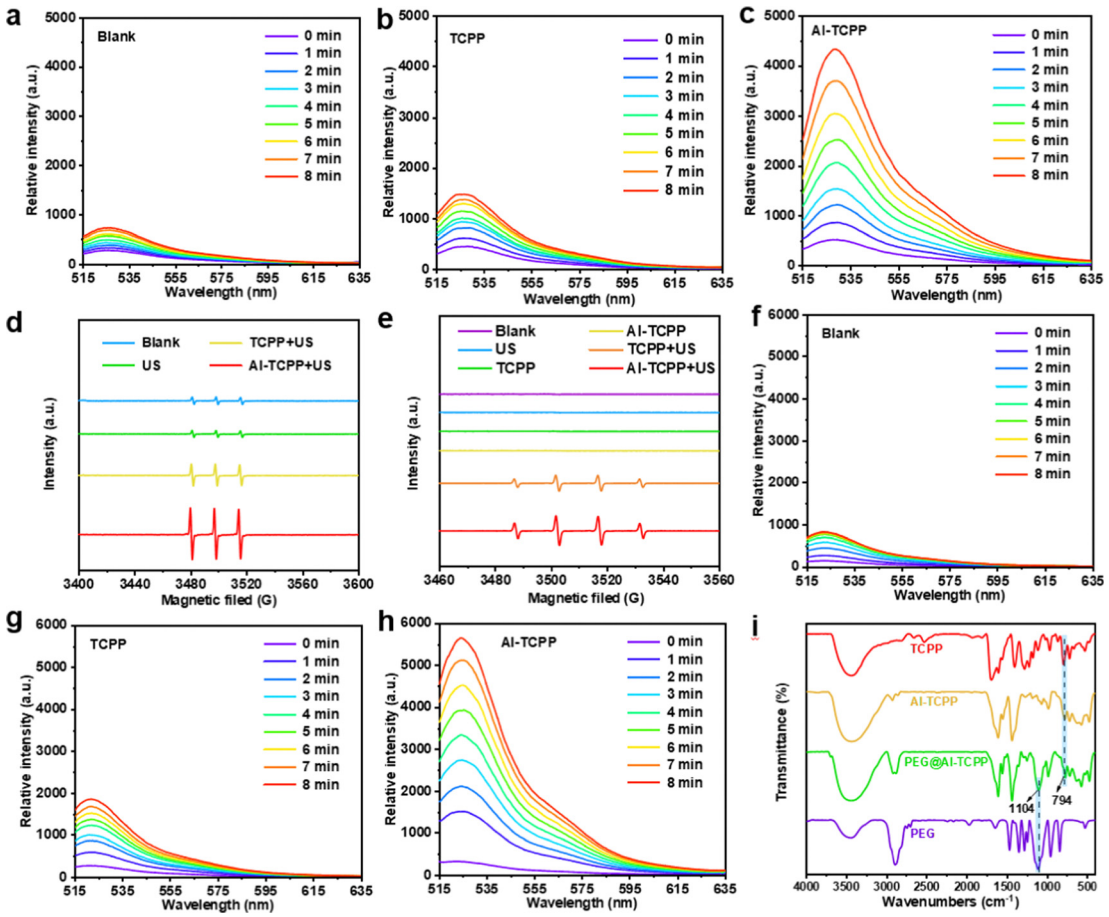

Fig. 3 The fluorescence spectra of (a–c) SOSG and (f–h) DCFH-DA in the presence of a blank sample, TCPP (50 μg mL^{-1}), and Al-TCPP (50 μg mL^{-1}) under US (50 kHz, 1.6 W cm^{-2}, 8 min) irradiation. (d) The TEMP/$^1O_2$ ESR spectra of a blank sample, US, TCPP + US, and Al-TCPP + US. (e) The DMPO/·OH ESR spectra of a blank sample, US, TCPP + US, and Al-TCPP + US. (i) FT-IR spectra of TCPP, Al-TCPP, PEG@Al-TCPP, and PEG.

oxygen sensor green (SOSG). As shown in Fig. 3a–c, the TCPP molecules exhibited very poor activity for $^1O_2$ generation under US irradiation, as demonstrated by the weak SOSG fluorescence intensity that was observed. In contrast, the Al-TCPP nanosheets resulted in an apparent increase in the fluorescence intensity of SOSG under US irradiation (Fig. 3c), indicating the enhanced SDT performance of Al-TCPP. Electron spin resonance (ESR) spectroscopy is considered to be the most sensitive evidence for detecting ROS generation. In view of this, the generation of $^1O_2$ mediated by Al-TCPP nanosheets was further validated using ESR with 2,2,6,6-tetramethylpiperidine (TEMP) as the $^1O_2$ trapping agent. As depicted in Fig. 3d, compared with the negligible $^1O_2$ (1 : 1 : 1) signal for the blank sample and the US group, an obvious $^1O_2$ (1 : 1 : 1) signal was found in the TCPP group. The signal intensity of the Al-TCPP nanosheets was significantly stronger than that of TCPP, which is consistent with the results of the SOSG assay. Since the cavitation effect of the US could induce •OH generation, we further evaluated the generation of •OH using ESR with 5,5-dimethyl-1-pyrroline N-oxide (DMPO) under different conditions. After exposure to US irradiation, a characteristic •OH (1 : 2 : 2 : 1) signal could be clearly observed for the TCPP and Al-TCPP nanosheets samples, and the Al-TCPP nanosheets demonstrated the best activity to generate •OH (Fig. 3e). Based on these results, the generation of total ROS was further examined using 2′,7′-dichlorodihydrofluorescein diacetate (DCFH-DA) as the probe molecule (Fig. 3f–h). It was found that TCPP produced a very small amount of ROS under US irradiation, while an elevated amount of ROS was observed for the Al-TCPP nanosheets under the same conditions, indicating the evident catalytic activity of Al-TCPP nanosheets for the generation of ROS. The above results proved that the Al-TCPP nanosheets could be used as a highly active SDT agent.

In order to achieve better biocompatibility, the Al-TCPP nanosheets were modified with PEG (denoted as PEG@Al-TCPP). Fourier transform infrared (FT-IR) spectroscopy was used to confirm the successful modification of Al-TCPP with PEG. As presented in Fig. 3i, the spectra of TCPP, Al-TCPP and PEG@Al-TCPP showed a strong absorption peak at 794 cm^{-1}, which is attributed to the para substitute on the benzene ring. The characteristic absorption band of PEG at 1104 cm^{-1} (C–O vibration absorption peak) could be detected in the PEG and PEG@Al-TCPP spectra, indicating the successful combination of PEG and the Al-TCPP nanosheets.

Encouraged by the remarkable ROS generation efficiency seen above, the *in vitro* SDT performance of the PEG@Al-TCPP nanosheets was investigated. First, the cellular uptake of the

PEG@Al-TCPP nanosheets was studied. 4T1 cells were incubated with Rhodamine B (RhB)-labeled PEG@Al-TCPP nanosheets for different periods of time (Fig. S7, ESI†). A strong red fluorescence was observed in the cytoplasm at 8 h, confirming the efficient endocytosis of PEG@Al-TCPP by the 4T1 cells. With the extension of the co-culture time to 12 h and 24 h, the red fluorescence intensity decreased significantly due to the gradual decomposition of the PEG@Al-TCPP nanosheets. Next, the biocompatibility of the PEG@Al-TCPP nanosheets was assessed in 4T1 cells *via* a methyl thiazolyl tetrazolium (MTT) assay. As shown in Fig. 4a, after incubation with 4T1 cells for 24 h, the PEG@Al-TCPP nanosheets had no obvious cytotoxic effect on the cells even at concentrations of up to 100 μg mL^{-1}, indicating their potential safety and good biocompatibility. A hemolysis analysis was also conducted on mouse red blood cells (RBCs) to further verify the biocompatibility of the PEG@Al-TCPP nanosheets (Fig. 4b and Fig. S8, ESI†). After 4 h of incubation, the hemolysis rates of all groups with different concentrations (5, 10, 20, 50, 100 μg mL^{-1}) were lower than the national standard (5%), indicating that the PEG@Al-TCPP nanosheets had no obvious hemolysis activity.

Subsequently, the cell-killing efficiency of the PEG@Al-TCPP nanosheets under US irradiation was also quantitatively evaluated *via* MTT assay. Fig. 4c reveals that blank sample, US, PEG@TCPP, and PEG@Al-TCPP did not exhibit obvious cytotoxicity toward the 4T1 cells, while about 50% of the cells survived when treated with PEG@TCPP (50 μg mL^{-1}) + US (50 kHz, 1.6 W cm^{-2}, 6 min), verifying the limited cytotoxicity of PEG@TCPP. In sharp contrast, the cytotoxicity of the PEG@Al-TCPP nanosheets was nearly 90%, which indicated that the SDT efficiency of TCPP was remarkably enhanced by its highly ordered assembly with Al^{3+}. In order to visualize the *in vitro* SDT effect, live/dead double-staining experiments were carried out (Fig. 4d). Compared with the negligible red fluorescence in the blank sample, US, PEG@TCPP, and PEG@Al-TCPP groups, the slight red fluorescence in PEG@TCPP + US group, and a high percentage of cell death with strong red fluorescence was observed in the 4T1 cells treated with PEG@Al-TCPP + US irradiation, which was consistent with the MTT results. In addition, 4T1 cells were stained with annexin V-FITC (Fluorescein Isothiocyanate) and propidium iodide (PI) for flow cytometric analysis to study the cell apoptosis induced by the PEG@Al-TCPP nanosheets (Fig. 4e). Compared with blank

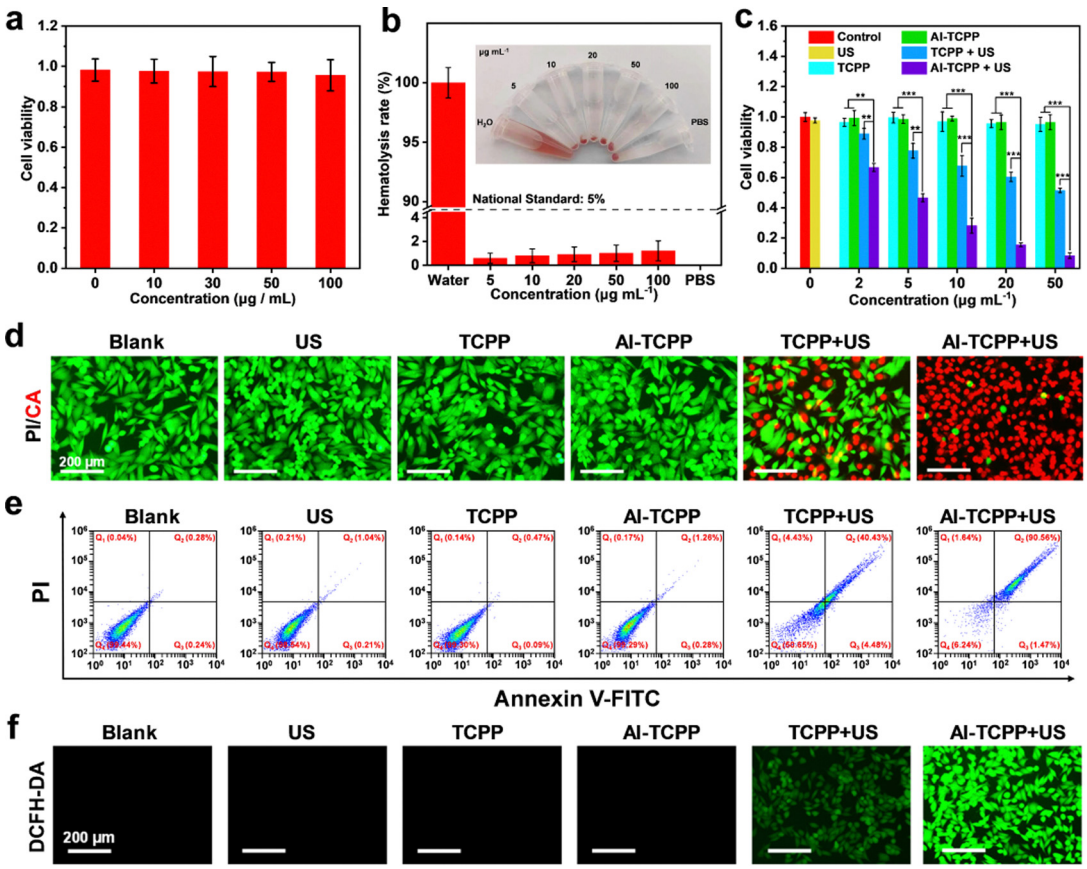

Fig. 4 (a) MTT assay of cells viabilities incubated with PEG@Al-TCPP under different concentrations. (b) Red blood cell (RBC) hemolysis rates for different concentrations of PEG@Al-TCPP after 4 h of incubation. Inset: Photograph of the H_2O, PEG@Al-TCPP (5, 10, 20, 50, 100 μg mL^{-1}), and PBS samples from left to right. (c) *In vitro* cytotoxicity profiles of cells incubated with PEG@TCPP or PEG@Al-TCPP under different conditions. (d) Calcein-AM/PI staining images of cells exposed to different conditions: (1) blank sample, (2) US (50 kHz, 1.6 W cm^{-2} for 6 min), (3) PEG@TCPP (50 μg mL^{-1}), (4) PEG@Al-TCPP (50 μg mL^{-1}), (5) PEG@TCPP + US, and (6) PEG@Al-TCPP + US. (e) Cell apoptosis analysis using Annexin V-FITC/PI double staining method. (f) DCFH-DA staining images of cells after exposure to different treatments: blank sample, US, PEG@TCPP, PEG@Al-TCPP, PEG@TCPP + US, and PEG@Al-TCPP + US. Error bars represent ± s.d. (n = 3) (*p < 0.05, **p < 0.01, ***p < 0.001).

sample, US, PEG@TCPP, and PEG@Al-TCPP groups, where no obvious apoptosis occurred, the percentage of early and late apoptosis in the PEG@Al-TCPP + US group reached 1.47% and 90.56%, respectively, revealing the excellent SDT efficiency of PEG@Al-TCPP. Moreover, DCFH-DA was selected as the ROS probe to monitor the intracellular ROS level. In Fig. 4f, intense green fluorescence was detected only in the 4T1 cells treated with PEG@Al-TCPP + US irradiation. The US-irradiated PEG@TCPP group exhibited weak green fluorescence, while blank sample and the cells treated with US, PEG@TCPP and PEG@Al-TCPP showed negligible fluorescence. These results demonstrate obvious ROS generation by the PEG@Al-TCPP nanosheets under US irradiation, which could be attributed to the successful enhancement of the reaction activity by an ion coordination strategy.

The mitochondrial membrane potential (MMP) is an important indicator of cell apoptosis. Therefore, a 5,5′,6,6′-tetrachloro-1,1′,3,3′-tetraethylbenzimidazolyl-carbocyanine iodide (JC-1) staining assay was used to evaluate the MMP. As shown in Fig. S9 (ESI†), strong red fluorescence (JC-1 aggregates) was observed in blank sample, US, PEG@TCPP, and PEG@Al-TCPP groups, indicating that the mitochondria maintained good integrity. The US treatment caused a decrease in red fluorescence and an increase in green fluorescence (JC-1 monomers) in the PEG@TCPP + US group, implying that the mitochondrial membrane was disrupted. Furthermore, the green fluorescence of the PEG@Al-TCPP + US group was obviously enhanced compared with the PEG@TCPP + US group, suggesting greater mitochondrial depolarization occurred in the former group.

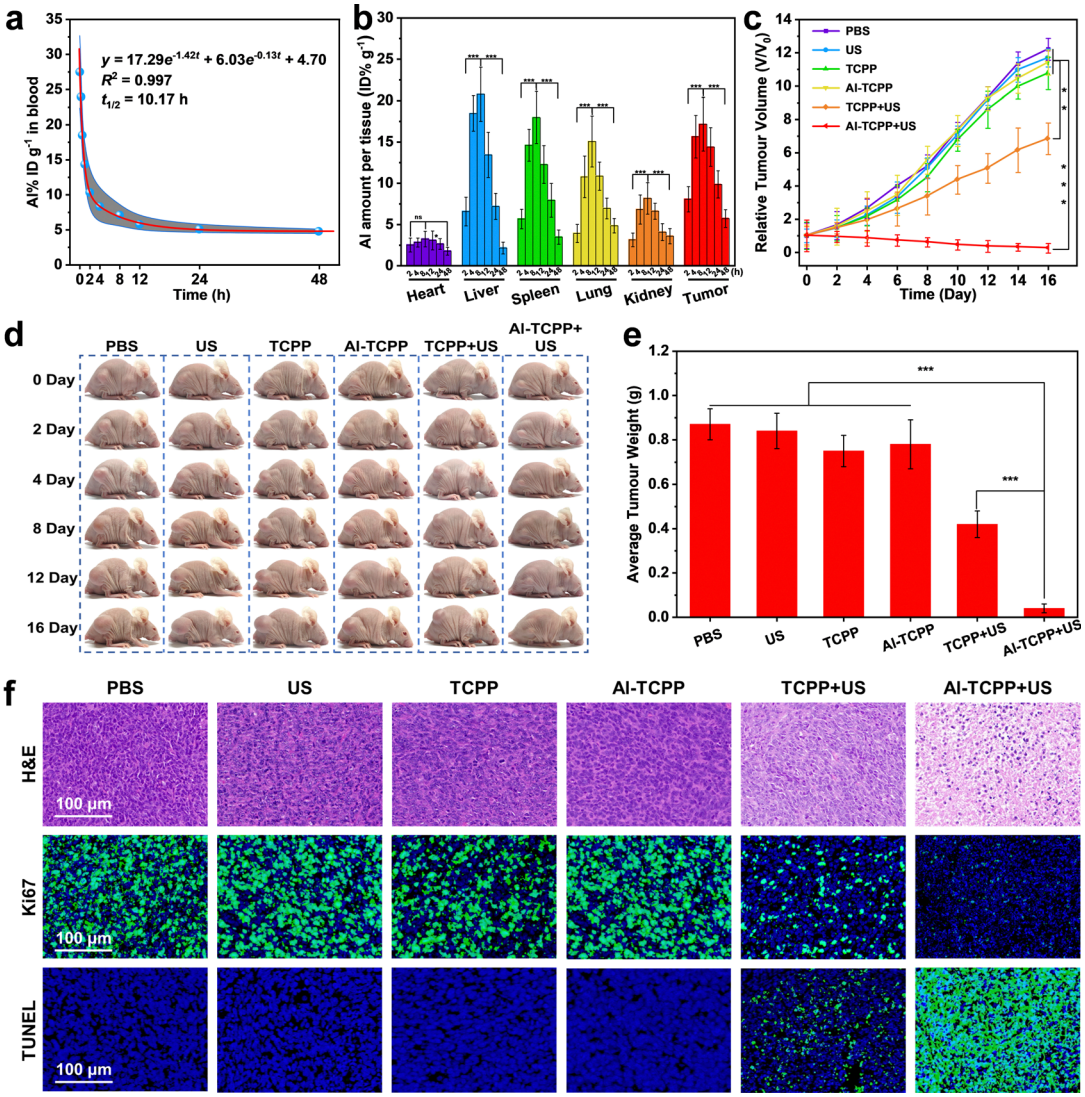

Fig. 5 (a) Blood circulation time and (b) quantitative biodistribution analysis of PEG@Al-TCPP in mice obtained by measuring the Al amount at different time points post-injection. (c) Tumor growth curves of mice following various treatments. Tumor sizes were normalized to their initial sizes (n = 6 per group). (d) Representative photographs of mice at different days post-treatment. (e) Corresponding average weight of tumors taken on day 16. (f) H&E, Ki67, and TUNEL staining assays performed on tumor tissue slices from different groups of mice 16 d post-treatment: (1) blank sample, (2) US (50 kHz, 1.6 W cm^{-2} for 6 min), (3) PEG@TCPP, (4) PEG@Al-TCPP, (5) PEG@TCPP + US, and (6) PEG@Al-TCPP + US. Error bars represent ± s.d. (n = 6) (*p < 0.05, **p < 0.01, ***p < 0.001).

We also used acridine orange (AO) as an indicator of SDT-mediated lysosome destruction to analyze the lysosome integrity (Fig. S10, ESI†). For the blank sample and the 4T1 cells treated with US, PEG@TCPP, and PEG@Al-TCPPs, a strong red AO fluorescence was observed. In contrast, the red AO fluorescence was significantly weakened in the PEG@TCPP + US (50 kHz, 1.6 W cm^{-2}, 6 min) group and almost disappeared in the PEG@Al-TCPP + US group, demonstrating severe oxidative damage to the 4T1 cells, accompanied by the destruction of lysosome integrity.

Based on the excellent *in vitro* SDT results, *in vivo* SDT anticancer experiments were conducted on 4T1 tumor-bearing mice. First, the blood circulation half-life of the PEG@Al-TCPP nanosheets was studied and calculated to be 10.17 h using a pharmacokinetic model (Fig. 5a). The long blood circulation time is beneficial for the accumulation of PEG@Al-TCPP at the tumor site. Then, the time-dependent biodistribution of PEG@Al-TCPP in the major organs (heart, liver, spleen, lung, and kidney) and the tumors was quantitatively determined using inductively coupled plasma mass spectroscopy (ICP-MS). As shown in Fig. 5b, the PEG@Al-TCPP nanosheets preferentially accumulated in the liver, spleen, lung, and tumor. The intratumor amount gradually increased to 17.15% at 8 h post-injection and remained as high as 5.73%, even at 48 h, ensuring a lasting anti-tumor effect.

After evaluating the accumulation of PEG@Al-TCPP at the tumor site, the *in vivo* SDT performance was further investigated in Balb/c nude mice. When the tumor volume reached 80 mm^3, the 4T1 tumor-bearing mice were randomly divided into six groups that would be exposed to the following treatments: (1) PBS (control), (2) US (50 kHz, 1.6 W cm^{-2}, 6 min), (3) PEG@TCPP, (4) PEG@Al-TCPP, (5) PEG@TCPP + US, and (6) PEG@Al-TCPP + US. As indicated by the tumor growth kinetics shown in Fig. 5c, compared with the PBS, US, PEG@TCPP, and PEG@Al-TCPP groups, the PEG@TCPP + US group showed partial inhibition of tumor growth. In contrast, the PEG@Al-TCPP + US group showed significant inhibition of tumor growth, demonstrating its excellent anticancer activity. The representative photos of the corresponding mice clearly verified the above results (Fig. 5d). After 16 days of treatment, all tumor tissues were collected and weighed (Fig. 5e). The average weight of the tumors further confirmed that treatment with PEG@Al-TCPP + US could effectively inhibit tumor growth.

Subsequently, the *in vivo* ROS generation ability of PEG@Al-TCPP was evaluated *via* a dihydroethidium (DHE) staining assay. As presented in Fig. S11 (ESI†), the DHE staining image obtained from the PEG@Al-TCPP + US group showed the strongest red fluorescence, indicating that PEG@Al-TCPP + US could generate a large amount of ROS and achieve excellent tumor cell destruction. To further explore the *in vivo* therapeutic mechanism of PEG@Al-TCPP, hematoxylin and eosin (H&E) and Ki-67 staining assays were performed on the tumor slices (Fig. 5f). Of all the groups, the most obvious nuclei contraction and the weakest green fluorescence were observed in the group treated with PEG@Al-TCPP + US, proving that enhanced SDT with PEG@Al-TCPP holds the potential to damage tumor cells and inhibit cell proliferation. Additionally, a terminal deoxynucleotidyl transferase (TdT)-mediated deoxyuridine triphosphate (dUTP) nick end labeling (TUNEL) staining assay was also performed on the tumor slices to study the apoptosis of the tumor cells. In Fig. 5f, the PEG@Al-TCPP + US group exhibited the highest positive TUNEL staining signal, indicating the fragmentation of DNA and the apoptosis of tumor cells.

As shown by the H&E staining of the major organs of the mice, no significant damage was observed after injection of the PEG@Al-TCPP nanosheets (Fig. S12, ESI†), and the standard blood, kidney and liver biochemical indexes remained normal at day 1 and day 16, suggesting that PEG@Al-TCPP causes negligible blood toxicity (Fig. S13, ESI†). Moreover, no obvious variation of body weight was detected in any of the mice groups during the treatments (Fig. S14, ESI†). These results collectively demonstrated that PEG@Al-TCPP has good biological safety and could be used for *in vivo* SDT. Furthermore, using ICP-MS, the excretion behaviors of the mice were studied by determining the Al content in feces and urine after intravenous injection of PEG@Al-TCPP. A high concentration of Al was found at 8 h and then gradually decreased to low concentration at 48 h (Fig. S15, ESI†), suggesting that PEG@Al-TCPP could be metabolized out of the body through the urine and feces.

Conclusions

In summary, we have prepared 2D Al-TCPP MOF nanosheets, *via* a facile solvothermal synthesis method that uses the appropriate ratio of organic solvent and water, for highly efficient sonodynamic cancer therapy. Al-TCPP MOF nanosheets with different morphologies could be obtained by only changing the composition of the reaction solvent and without the need for any surfactants. Promisingly, the performance of the 2D Al-TCPP nanosheets for both $^1O_2$ and $^{\bullet}OH$ generation under US irradiation is significantly enhanced when the organic TCPP molecules are embedded into the MOF framework. After modification with PEG, the PEG@Al-TCPP nanosheets exhibited excellent performance when used as a sonosensitizer in SDT to kill cancer cells and eliminate malignant tumors. Our study has proven that 2D MOF nanosheets can be used as efficient sonosensitizers for sonodynamic cancer therapy, and they may also be promising for antibacterial therapies.

Author contributions

Z. Z., L. M., M. Z., R. L., and C. T. designed and initiated the project. Z. Z. synthesized and characterized the 2D Al-TCPP nanosheets. T. W. and T. H. conducted therapeutic studies on the cells and animals. S. Y. and H. L. performed the AFM characterization of the 2D Al-TCPP nanosheets. C. C. and S. L. helped with the synthesis and characterization of the 2D Al-TCPP nanosheets. Z. Z., T. H., L. M., M. Z. R. L., and C. T. cowrote the paper and all authors contributed to the discussion and preparation of the manuscript.

Conflicts of interest

The authors declare no competing financial interests.

Acknowledgements

This work is supported by the National Natural Science Foundation of China (52102348 and 22171123), and the Science and Technology Innovation Talent Program of University in Henan Province (23HASTIT016). C. T. thanks the funding support from the National Natural Science Foundation of China (22005259) and the Start-Up Grant (Project No. 9610495) from City University of Hong Kong. R. L. thanks the funding support from National Natural Science Foundation of China (21971007) and the Beijing Natural Science Foundation (2212044). M. Z. thanks the funding support from the National Natural Science Foundation of China (21905195), Natural Science Foundation of Tianjin City (20JCYBJC00800), and the PEIYANG Young Scholars Program of Tianjin University (2020XRX-0023).

References

1 S. Son, J. Kim, X. Wang, C. Zhang, S. Yoon, J. Shin, A. Sharma, M. Lee, L. Cheng, J. Wu and J. Kim, Multifunctional sonosensitizers in sonodynamic cancer therapy, *Chem. Soc. Rev.*, 2020, **49**, 3244–3261.

2 Z. Xiao, Q. Chen, Y. Yang, S. Tu, B. Wang, Y. Qiu, Y. Jiang, Q. Huang and K. Ai, State of the art advancements in sonodynamic therapy (SDT): Metal-Organic frameworks for SDT, *Chem. Eng. J.*, 2022, **449**, 137889.

3 Y. Yang, X. Wang, H. Qian and L. Cheng, Titanium-based sonosensitizers for sonodynamic cancer therapy, *Appl. Mater. Today*, 2021, **25**, 101215.

4 X. Pan, N. Wu, S. Tian, J. Guo, C. Wang, Y. Sun, Z. Huang, F. Chen, Q. Wu, Y. Jing, Z. Yin, B. Zhao, X. Xiong, H. Liu and D. Zhou, Inhalable MOF-derived nanoparticles for sonodynamic therapy of bacterial pneumonia, *Adv. Funct. Mater.*, 2022, **32**, 2112245.

5 X. Qian, Y. Zheng and Y. Chen, Micro/nanoparticle-augmented sonodynamic therapy (SDT): Breaking the depth shallow of photoactivation, *Adv. Mater.*, 2016, **28**, 8097–8129.

6 H. Chen, X. He, Z. Zhou, Z. Wu, H. Li, X. Peng, Y. Zhou, C. Tan and J. Shen, Metallic phase enabling MoS_2 nanosheets as an efficient sonosensitizer for photothermal-enhanced sonodynamic antibacterial therapy, *J. Nanobiotechnol.*, 2022, **20**, 136.

7 X. He, J. Hou, X. Sun, P. Jangili, J. An, Y. Qian, J. S. Kim and J. Shen, NIR-II photo-amplified sonodynamic therapy using sodium molybdenum bronze nanoplatform against subcutaneous staphylococcus aureus infection, *Adv. Funct. Mater.*, 2022, **32**, 2203964.

8 Z. Wang, B. Liu, Q. Sun, L. Feng, F. He, P. Yang, S. Gai, Z. Quan and J. Lin, Upconverted metal-organic framework janus architecture for near-infrared and ultrasound Co-enhanced high performance tumor therapy, *ACS Nano*, 2021, **15**, 12342–12357.

9 W. Shen, T. Hu, X. Liu, J. Zha, F. Meng, Z. Wu, Z. Cui, Y. Yang, H. Li, Q. Zhang, L. Gu, R. Liang and C. Tan, Defect engineering of layered double hydroxide nanosheets as inorganic photosensitizers for NIR-III photodynamic cancer therapy, *Nat. Commun.*, 2022, **13**, 3384.

10 T. Hu, Z. Gu, G. R. Williams, M. Strimaite, J. Zha, Z. Zhou, X. Zhang, C. Tan and R. Liang, Layered double hydroxide-based nanomaterials for biomedical applications, *Chem. Soc. Rev.*, 2022, **51**, 6126–6176.

11 S. Liang, X. Xiao, L. Bai, B. Liu, M. Yuan, P. Ma, M. Pang, Z. Cheng and J. Lin, Conferring Ti-based MOFs with defects for enhanced sonodynamic cancer therapy, *Adv. Mater.*, 2021, **33**, 2100333.

12 J. Zhou, D. Xu, G. Tian, Q. He, X. Zhang, J. Liao, L. Mei, L. Chen, L. Gao, L. Zhao, G. Yang, W. Yin, G. Nie and Y. Zhao, Coordination-driven self-assembly strategy-activated Cu single-atom nanozymes for catalytic tumor-specific therapy, *J. Am. Chem. Soc.*, 2023, **145**, 4279–4293.

13 Z. Zhou, X. Li, T. Hu, B. Xue, H. Chen, L. Ma, R. Liang and C. Tan, Molybdenum-Based nanomaterials for photothermal cancer therapy, *Adv. NanoBiomed Res.*, 2022, **2**, 2200065.

14 X. Wang, X. Zhong, L. Bai, J. Xu, F. Gong, Z. Dong, Z. Yang, Z. Zeng, Z. Liu and L. Cheng, Ultrafine titanium monoxide (TiO_{1+x}) nanorods for enhanced sonodynamic therapy, *J. Am. Chem. Soc.*, 2020, **142**, 6527–6537.

15 F. Gong, L. Cheng, N. Yang, Y. Gong, Y. Ni, S. Bai, X. Wang, M. Chen, Q. Chen and Z. Liu, Preparation of $TiH_{1.924}$ nanodots by liquid-phase exfoliation for enhanced sonodynamic cancer therapy, *Nat. Commun.*, 2020, **11**, 3712.

16 X. Wang, X. Wang, Q. Yue, H. Xu, X. Zhong, L. Sun, G. Li, Y. Gong, N. Yang, Z. Wang, Z. Liu and L. Cheng, Liquid exfoliation of TiN nanodots as novel sonosensitizers for photothermal-enhanced sonodynamic therapy against cancer, *Nano Today*, 2021, **39**, 101170.

17 Z. Zhou, Y. Wang, F. Peng, F. Meng, J. Zha, L. Ma, Y. Du, N. Peng, L. Ma, Q. Zhang, L. Gu, W. Yin, Z. Gu and C. Tan, Intercalation-activated layered MoO_3 nanobelts as biodegradable nanozymes for tumor-specific photo-enhanced catalytic therapy, *Angew. Chem., Int. Ed.*, 2022, **61**, 202115939.

18 X. Pan, W. Wang, Z. Huang, S. Liu, J. Guo, F. Zhang, H. Yuan, X. Li, F. Liu and H. Liu, MOF-derived double-layer hollow nanoparticles with oxygen generation ability for multimodal imaging-guided sonodynamic therapy, *Angew. Chem., Int. Ed.*, 2020, **59**, 13557–13561.

19 W. Um, P. K. EK, J. Lee, C. Kim, D. You and J. Park, Recent advances in nanomaterial-based augmented sonodynamic therapy of cancer, *Chem. Commun.*, 2021, **57**, 2854–2866.

20 J. Ouyang, Z. Tang, N. Farokhzad, N. Kong, N. Kim, C. Feng, S. Blake, Y. Xiao, C. Liu, T. Xie and W. Tao, Ultrasound mediated therapy: Recent progress and challenges in nanoscience, *Nano Today*, 2020, **35**, 100949.

21 Z. Dong, L. Feng, Y. Hao, Q. Li, M. Chen, Z. Yang, H. Zhao and Z. Liu, Synthesis of $CaCO_3$-based nanomedicine for enhanced sonodynamic therapy via amplification of tumor oxidative stress, *Chem*, 2020, **6**, 1391–1407.

22 J. Cao, Y. Sun, C. Zhang, X. Wang, Y. Zeng, T. Zhang and P. Huang, Tablet-like TiO_2/C nanocomposites for repeated

type I sonodynamic therapy of pancreatic cancer, *Acta Biomater.*, 2021, **129**, 269–279.

23 Y. Pu, H. Yin, C. Dong, H. Xiang, W. Wu, B. Zhou, D. Du, Y. Chen and H. Xu, Sono-controllable and ROS-sensitive CRISPR-cas9 genome editing for augmented/synergistic ultrasound tumor nanotherapy, *Adv. Mater.*, 2021, **33**, 2104641.

24 X. Xing, S. Zhao, T. Xu, L. Huang, Y. Zhang, M. Lan, C. Lin, X. Zheng and P. Wang, Advances and perspectives in organic sonosensitizers for sonodynamic therapy, *Coord. Chem. Rev.*, 2021, **445**, 214087.

25 M. Lan, S. Zhao, W. Liu, C. Lee, W. Zhang and P. Wang, Photosensitizers for photodynamic therapy, *Adv. Healthcare Mater.*, 2019, **8**, 1900132.

26 L. Dang, T. Zhang, T. Chen, Y. Zhao, C. Zhao, F. Aznarez, K. Sun and L. Ma, Coordination assembly and NIR photothermal conversion of Cp*Rh-based supramolecular topologies based on distinct conjugated systems, *Org. Chem. Front.*, 2022, **9**, 5505–5515.

27 L. Zhang, H. Yi, J. Song, J. Huang, K. Yang, B. Tan, D. Wang, N. Yang, Z. Wang and X. Li, Mitochondria-targeted and ultrasound-activated nanodroplets for enhanced deep-penetration sonodynamic cancer therapy, *ACS Appl. Mater. Interfaces*, 2019, **11**, 9355–9366.

28 X. Zheng, W. Liu, J. Ge, Q. Jia, F. Nan, Y. Ding, J. Wu, W. Zhang, C. Lee and P. Wang, Biodegradable natural product-based nanoparticles for near-infrared fluorescence imaging-guided sonodynamic therapy, *ACS Appl. Mater. Interfaces*, 2019, **11**, 18178–18185.

29 H. Chen, X. Guan, Q. Liu, L. Yang, J. Guo, F. Gao, Y. Qi, X. Wu, F. Zhang and X. Tian, Co-assembled nanocarriers of de novo thiol-activated hydrogen sulfide donors with an RGDFF pentapeptide for targeted therapy of non-small-cell lung cancer, *ACS Appl. Mater. Interfaces*, 2022, **14**, 53475–53490.

30 A. Ma, H. Chen, Y. Cui, Z. Luo, R. Liang, Z. Wu, Z. Chen, T. Yin, J. Ni, M. Zheng and L. Cai, Metalloporphyrin complex-based nanosonosensitizers for deep-tissue tumor theranostics by noninvasive sonodynamic therapy, *Small*, 2019, **15**, 1804028.

31 X. Zhao, X. He, A. Hou, C. Cheng, X. Wang, Y. Yue, Z. Wu, H. Wu, B. Liu, H. Li, J. Shen, C. Tan, Z. Zhou and L. Ma, Growth of Cu_2O nanoparticles on two-dimensional Zr-ferrocene-metal-organic framework nanosheets for photothermally enhanced chemodynamic antibacterial therapy, *Inorg. Chem.*, 2022, **61**, 9328–9338.

32 L. Dang, T. Li, T. Zhang, Y. Zhao, T. Chen, X. Gao, L. Ma and G. Jin, Highly selective synthesis and near-infrared photothermal conversion of metalla-borromean ring and [2]catenane assemblies, *Chem. Sci.*, 2022, **13**, 5130–5140.

33 P. Gao, Y. Jiang, H. Liu, M. Zhou, T. Li, H. Fu, L. Ma and D. Li, Pillar-layer chiral MOFs as a crystalline platform for circularly polarized luminescence and single-phase white-light emission, *ACS Appl. Mater. Interfaces*, 2022, **14**, 16435–16444.

34 Y. Qin, Y. Wan, J. Guo and M. Zhao, Two-dimensional metal–organic framework nanosheet composites: Preparations and applications, *Chin. Chem. Lett.*, 2022, **33**, 693–702.

35 Y. Qin, J. Guo and M. Zhao, Metal-organic framework-based solid acid materials for biomass upgrade, *Trans. Tianjin Univ.*, 2021, **27**, 434–449.

36 Z. Li, J. Guo, Y. Wan, Y. Qin and M. Zhao, Combining metal-organic frameworks (MOFs) and covalent-organic frameworks (COFs): Emerging opportunities for new materials and applications, *Nano Res.*, 2022, **15**, 3514–3532.

37 J. Zhu, X. Chen, A. Q. Thang, F.-L. Li, D. Chen, H. Geng, X. Rui and Q. Yan, Vanadium-based metal-organic frameworks and their derivatives for electrochemical energy conversion and storage, *SmartMat*, 2022, **3**, 384–416.

38 X. Li, X. Zhao, D. Chu, X. Zhu, B. Xue, H. Chen, Z. Zhou and J. Li, Silver nanoparticle-decorated 2D Co-TCPP MOF nanosheets for synergistic photodynamic and silver ion antibacterial, *Surf. Interfaces*, 2022, **33**, 102247.

39 Q. Ding, Z. Xu, L. Zhou, C. Rao, W. Li, M. Muddassir, H. Sakiyama, B. Li, Q. Ouyang and J. Liu, A multimodal metal-organic framework based on unsaturated metal site for enhancing antitumor cytotoxicity through chemo-photodynamic therapy, *J. Colloid Interface Sci.*, 2022, **621**, 180–194.

40 M. Li, S. Yin, M. Lin, X. Chen, Y. Pan, Y. Peng, J. Sun, A. Kumar and J. Liu, Current status and prospects of metal-organic frameworks for bone therapy and bone repair, *J. Mater. Chem. B*, 2022, **10**, 5105–5128.

41 F. Dong, High-performance single-atom implanted metal-organic framework/MnO_2 for NO_x oxidation in plasma, *Acta Phys.-Chim. Sin.*, 2021, **37**, 2010074.

42 Y. Sun, M. Gao, H. Li, L. Xu, Q. Xue, X. Wang, Y. Bai and C. Wu, Application of metal-organic frameworks to the interface of lithium metal batteries, *Acta Phys.-Chim. Sin.*, 2021, **37**, 2007048.

43 S. Jiang, Q. He, C. Li, K. Dang, L. Ye, W. Zhang and Y. Tian, Employing the thiol-ene click reaction via metal-organic frameworks for integrated sonodynamic-starvation therapy as an oncology treatment, *Sci. China Mater.*, 2021, **65**, 1112–1121.

44 P. Geng, N. Yu, X. Liu, Q. Zhu, M. Wen, Q. Ren, P. Qiu, H. Zhang, M. Li and Z. Chen, Sub 5 nm Gd (3 +)-hemoporfin framework nanodots for augmented sonodynamic theranostics and fast renal clearance, *Adv. Healthcare Mater.*, 2021, **10**, 2100703.

45 K. Zhang, X. Meng, Z. Yang, H. Dong and X. Zhang, Enhanced cancer therapy by hypoxia-responsive copper metal-organic frameworks nanosystem, *Biomaterials*, 2020, **258**, 120278.

46 F. Zhuang, Q. Ma, C. Dong, H. Xiang, Y. Shen, P. Sun, C. Li, Y. Chen, B. Lu, Y. Chen and B. Huang, Sequential ultrasound-triggered and hypoxia-sensitive nanoprodrug for cascade amplification of sonochemotherapy, *ACS Nano*, 2022, **16**, 5439–5453.

47 C. Meng, Y. Cao, Y. Luo, F. Zhang, Q. Kong, A. Alshehri, K. Alzahrani, T. Li, Q. Liu and X. Sun, A Ni-MOF nanosheet array for efficient oxygen evolution electrocatalysis in alkaline media, *Inorg. Chem. Front.*, 2021, **8**, 3007–3011.

48 Z. Deng, C. Ma, S. Yan, K. Dong, Q. Liu, Y. Luo, Y. Liu, J. Du, X. Sun and B. Zheng, One-dimensional conductive metal-

organic framework nanorods: a highly selective electrocatalyst for the oxygen reduction to hydrogen peroxide, *J. Mater. Chem. A*, 2021, **9**, 20345–20349.

49 J. Gu, Y. Peng, T. Zhou, J. Ma, H. Pang and Y. Yamauchi, Porphyrin-based framework materials for energy conversion, *Nano Res. Energy*, 2022, **1**, 9120009.

50 K. Dong, J. Liang, Y. Ren, Y. Wang, Z. Xu, L. Yue, T. Li, Q. Liu, Y. Luo, Y. Liu, S. Gao, M. Hamdy, Q. Li, D. Ma and X. Sun, Electrochemical two-electron O_2 reduction reaction toward H_2O_2 production: using cobalt porphyrin decorated carbon nanotubes as a nanohybrid catalyst, *J. Mater. Chem. A*, 2021, **9**, 26019–26027.

51 K. Dong, J. Liang, Y. Wang, L. Zhang, Z. Xu, S. Sun, Y. Luo, T. Li, Q. Liu, N. Li, B. Tang, A. Alshehri, Q. Li, D. Ma and X. Sun, Conductive two-dimensional magnesium metal-organic frameworks for high-efficiency O_2 electroreduction to H_2O_2, *ACS Catal.*, 2022, **12**, 6092–6099.

52 X. Zhao, H. Qiu, Y. Shao, P. Wang, S. Yu, H. Li, Y. Zhou, Z. Zhou, L. Ma and C. Tan, Silver nanoparticle-modified 2D MOF nanosheets for photothermally enhanced silver ion release antibacterial treatment, *Acta Phys.-Chim. Sin.*, 2023, **39**, 2211043.

53 B. Xue, X. Geng, H. Cui, H. Chen, Z. Kang, H. Chen, H. Li, Z. Zhou, M. Zhao, C. Tan and J. Li, Size engineering of 2D MOF nanosheets for enhanced photodynamic antimicrobial therapy, *Chin. Chem. Lett.*, 2023, DOI: 10.1016/j.cclet.2023.108140.

54 H. Xu, N. Yu, J. Zhang, Z. Wang, P. Geng, M. Wen, M. Li, H. Zhang and Z. Chen, Biocompatible Fe-hematoporphyrin coordination nanoplatforms with efficient sonodynamic-chemo effects on deep-seated tumors, *Biomaterials*, 2020, **257**, 120239.

55 C. Zhang, L. Xin, J. Li, J. Cao, Y. Sun, X. Wang, J. Luo, Y. Zeng, Q. Li, Y. Zhang, T. Zhang and P. Huang, Metal-organic framework (MOF)-based ultrasound-responsive dual-sonosensitizer nanoplatform for hypoxic cancer therapy, *Adv. Healthcare Mater.*, 2022, **11**, 2101946.

56 Y. Bao, J. Chen, H. Qiu, C. Zhang, P. Huang, Z. Mao and W. Tong, Erythrocyte membrane-camouflaged PCN-224 nanocarriers integrated with platinum nanoparticles and glucose oxidase for enhanced tumor sonodynamic therapy and synergistic starvation therapy, *ACS Appl. Mater. Interfaces*, 2021, **13**, 24532–24542.

57 W. Wang, X. Pan, H. Yang, H. Wang, Q. Wu, L. Zheng, B. Xu, J. Wang, X. Shi, F. Bai and H. Liu, Bioactive metal-organic frameworks with specific metal-nitrogen (M-N) active sites for efficient sonodynamic tumor therapy, *ACS Nano*, 2021, **15**, 20003–20012.

58 Q. Xu, G. Zhan, Z. Zhang, T. Yong, X. Yang and L. Gan, Manganese porphyrin-based metal-organic framework for synergistic sonodynamic therapy and ferroptosis in hypoxic tumors, *Theranostics*, 2021, **11**, 1937–1952.

59 T. Zhang, Y. Sun, J. Cao, J. Luo, J. Wang, Z. Jiang and P. Huang, Intrinsic nucleus-targeted ultra-small metal-organic framework for the type I sonodynamic treatment of orthotopic pancreatic carcinoma, *J. Nanobiotechnol.*, 2021, **19**, 315.

60 Y. Sun, J. Cao, X. Wang, C. Zhang, J. Luo, Y. Zeng, C. Zhang, Q. Li, Y. Zhang, W. Xu, T. Zhang and P. Huang, Hypoxia-Adapted sono-chemodynamic treatment of orthotopic pancreatic carcinoma using copper metal-organic frameworks loaded with an ultrasound-induced free radical initiator, *ACS Appl. Mater. Interfaces*, 2021, **13**, 38114–38126.

61 S. Liu, M. Wen, M. Huang, H. Wang, Z. Chen and N. Yu, Nanoscale hematoporphrin-based frameworks for photo-sono synergistic cancer therapy via utilizing Al(III) as metal nodes rather than heavy metals, *J. Colloid Interface Sci.*, 2022, **616**, 23–33.

62 W. Zhu, Q. Chen, Q. Jin, Y. Chao, L. Sun, X. Han, J. Xu, L. Tian, J. Zhang, T. Liu and Z. Liu, *Nano Res.*, 2021, **14**, 212–221.

63 A. Fateeva, P. Chater, C. Ireland, A. Tahir, Y. Khimyak, P. Wiper, J. Darwent and M. Rosseinsky, A water-stable porphyrin-based metal-organic framework active for visible-light photocatalysis, *Angew. Chem., Int. Ed.*, 2012, **51**, 7440–7444.